46.0 INFLUENCE OF MICROSTRUCTURE ON THE OXIDATION BEHAVIORS OF REFRACTORY COMPLEX CONCENTRATED ALLOYS (RCCAS)

Noah Welch (ISU)
Faculty: Peter Collins (ISU)
Industrial Mentor: Todd Butler (AFRL)

This project initiated in Fall 2020. The research performed during this project will serve as the basis for a Ph.D. thesis program for Noah Welch.

46.1 Project Overview and Industrial Relevance

Refractory complex concentrated alloys (RCCA) are a subclass of refractory high entropy alloys (RHEA), that have five or less principal alloying elements in a near-equimolar composition [46.1]. Due to a unique combination of properties, these alloys show great promise for future use in advanced, high temperature, structural applications [46.2]. In addition to reported high-temperature compressive strength, the complex arrangement of atomic constituents provides a unique framework for the design of inherent oxidation resistance that is not readily accessible in conventional refractory alloys [46.2-46.4]. The complex arrangement of elements leads to formation of complex oxide structures, halting oxidation kinetics and thus leading to much slower oxidation rates [46.1-46.2]. A relationship between microstructural parameters (grain size, morphology, precipitates, etc.) and oxide structure will be established to provide a framework to engineer these alloys further.

RCCAs often form single phase BCC structures or BCC + Laves intermetallic structures, depending on the concentration of constituents [46.5]. Multiple compositions in the TaTiCr system— TaTiCr, Ta_2TiCr, Ta_4Ti_3Cr, and Ta_4TiCr_3 (at%)—will be analyzed to understand compositional contributions to microstructure and oxidation properties. From these analyses, a composition range with the most desirable properties will be determined. This will be followed by heat treatment, thermomechanical processing, and alloying additions to alter the microstructure and oxide structure.

A novel, bicombinatorial method for relating composition and oxidation behavior will be used after narrowing down the most promising compositional range. A compositionally graded, additive manufactured specimen will be heated using a Gleeble thermal-mechanical simulation system. This will establish a temperature gradient orthogonal to the composition gradient, allowing rapid assessment of oxidation properties in relation to composition.

Attributing their comparable density, impressive high-temperature oxidation resistance, and overall higher operating temperature regime, these alloy systems could potentially displace and outperform current high-temperature, oxidation-resistant alloys—such as nickel-based superalloys—in specific applications. Despite their potential, research is required to establish an equivalent knowledge base regarding fundamental properties and their underlying mechanisms, including, but not limited to, oxidation mechanisms and behavior.

46.2 Previous Work

Scientists at the Air Force Research Laboratory (AFRL) have made significant progress researching oxidation and mechanical behavior of several RCCAs systems, including Nb, Ti, Zr, Cr, Al, Mo, and others [46.1-46.2]. Work published by Dr. Oleg Senkov and Dr. Dan Miracle [46.1-46.2, 46.4-46.5] have been especially influential in elucidating the mechanical and chemical properties as well as the broader potential impact for many RCCA and RHEA systems. A comprehensive database of properties, and microstructural information has been developed by Senkov, Miracle, et al., for over 370 RHEAs and RCCAs [46.6]. The most common structure observed in RCCAs is a single-phase disordered BCC structure [46.2]. This disordered structure induces lattice strain and leads to exceptionally high strength and low ductility at room temperature [46.2]. Laves (C14 or C15) is the second most common phase, generally associated with Cr, Mo, and Zr. From this information, and in conjunction with CALPHAD predictions, the TaTiCr system is expected to be composed of varying fractions of BCC+Laves, depending on specific composition ranges. Additionally, discussions with AFRL have shown that Ti additions effectively “invert” the microstructure from primary Laves to primary BCC. This is critical for the viability of a commercial alloy as the ductility can be increased considerably [46.3]. The oxidation behavior of NbTiZrCr

specifically influenced the choice to pursue the TaTiCr system, as Ta has excellent oxidation performance and the relation between Ti and Cr has a significant effect on the Laves-BCC phase ratios. Further, Butler et al [46.4] compares the NbTiZrV and NbTiZrCr systems and it can be seen that the oxidation performance of the Cr alloy far exceeds that of the V alloy. The V alloy was completely oxidized after a 100-hour test and the Cr alloy had bulk material remaining and far less mass gain. Analysis of the oxide structure for both alloys show that several complex oxide structures form after long-term oxidation tests, with the Cr alloy exhibiting a mix of both simple and complex oxides. The complexity of these structures is attributed to the heightened oxidation performance due to halting the kinetics of oxide formation deeper in the bulk. However, due to the discrepancy between oxidation performance when both alloys exhibited complex oxide structures, there is a need to characterize and model the oxidation mechanisms at play.

Previous work on this project has been primarily focused on characterizing the various alloys in the as-cast and HIP conditions. Twelve ingots were prepared via arc melting at the Ames Laboratory Metals Preparation center. Three of each of the following compositions were prepared: TaTiCr, Ta_2TiCr, Ta_4Ti_3Cr, and Ta_4TiCr_3. To maximize homogeneity, the specimens were Hot Isostatic Pressed (HIP) at AFRL. Specimens were made via Electrical Discharge Machining (EDM) for Thermal Gravitational Analysis (TGA), compression test, and metallography. To maximize homogeneity, all ingots were sent to AFRL to be hot isostatic pressed. The ingots were held at 1400°C for 3 hours at 30 ksi (~206 MPa).

Scanning Electron Microscopy (SEM) imaging, Energy Dispersive Spectroscopy (EDS), and X-ray Diffraction (XRD) techniques were used to gather microstructural, phase fraction, and phase composition data from the alloys. After HIP, three alloys (TaTiCr, Ta_2TiCr, and Ta_4TiCr_3) showed a BCC/Laves two-phase microstructure (**Fig. 46.1a, b, e-h**), with the Laves phase fraction directly correlated to the relative Cr content in each alloy; the Ta_4Ti_3Cr alloy consisted of single-phase BCC microstructure (**Figure 46.1c, d**). The phase compositions of the Laves phase remained relatively constant for each alloy; however, the BCC matrix composition was heavily influenced by the Ta;Ti ratio in each alloy, for example TaTiCr had a matrix composition of 28% Ta and 60% Ti, while the Ta_4TiCr_3 alloy had a matrix composition of 67% Ta and 20% Ti.

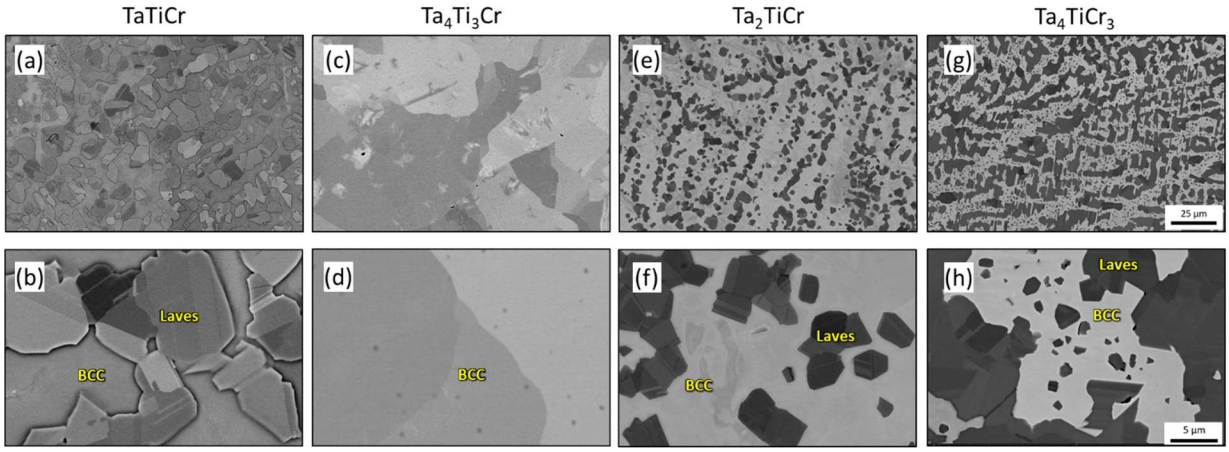

Figure 46.1: Backscatter SEM images of the microstructure of the four alloys after HIP for 3 hours at 1400°C and 207 MPa: (a,b) TaTiCr, (c,d) Ta_4Ti_3Cr, (e,f) Ta_2TiCr, and (g,h) Ta_4TiCr_3. Scale bars are consistent across each horizontal row

46.3 Recent Progress

46.3.1 Oxidation Tests

Oxidation tests were conducted on 3mm x 3mm cylindrical specimens excised from the HIP ingots using Electrical Discharge Machining (EDM). Specimens were tested for 24 hours in air at 1200°C (**Figure 46.2**). The alloy with the slowest kinetics was TaTiCr, with a specific mass change of 7.2 mg/cm^2 after 24 hours at 1200°C; the thin oxide

scale was dark grey, with brown regions along the edges of the cylinder. Ta_4TiCr_3, Ta_4Ti_3Cr, and Ta_2TiCr had specific mass changes of 71.5, 124.1, and 160.9mg/cm^2, respectively. TheTa_4TiCr_3 specimen had a dark green, rumpled scale that bulged slightly in the middle of the cylinder. The Ta_4Ti_3Cr specimen showed a thick, cracked orange scale that contained longitudinal splits along the length of the specimen. The Ta_2TiCr specimen was completely oxidized after 24 hours and had a thick brown scale that left no remaining metal after testing.

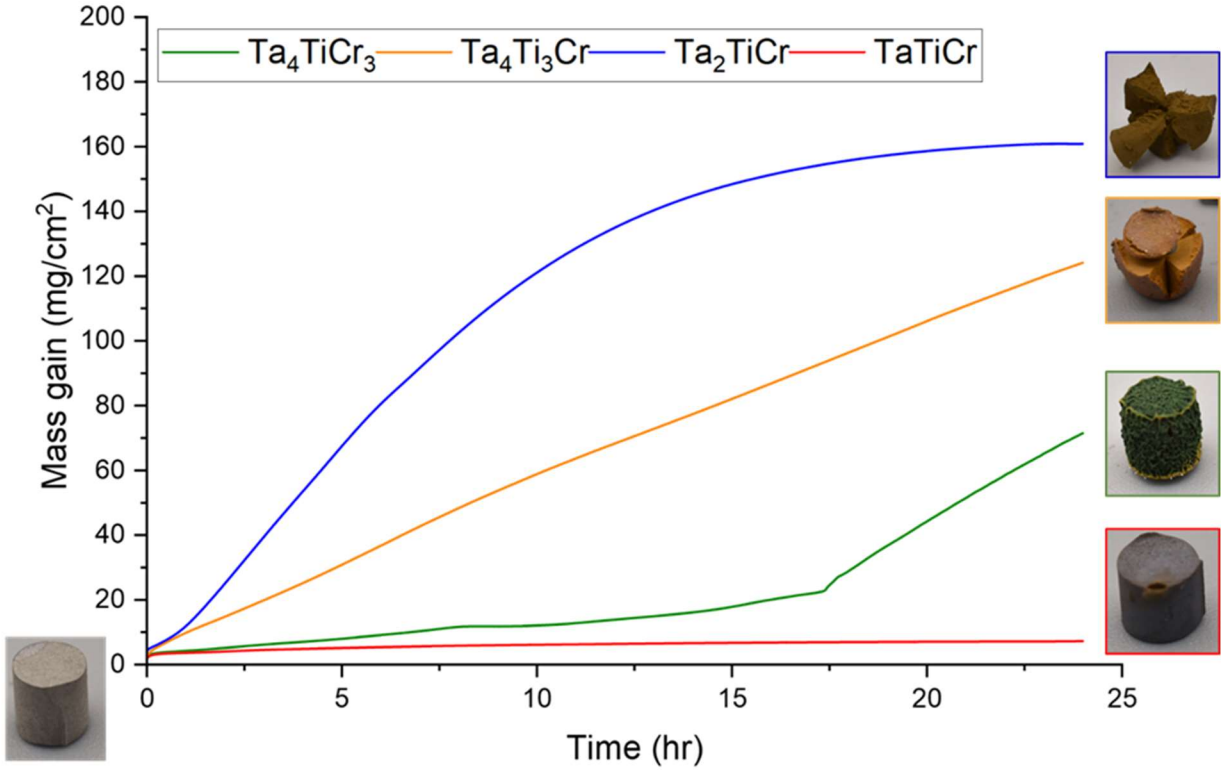

Figure 46.2: Specific mass change during the 1200 °C STA oxidation tests of TaTiCr, Ta_4Ti_3Cr, Ta_2TiCr, Ta_4TiCr_3. Specimen images were taken after 24 hours.

Oxidation kinetics were analyzed using a general growth rate law:

$$\Delta m = kt^n \tag{31.1}$$

where Δm is the specific mass change normalized to initial surface area (mg/cm^2), k is the rate constant, t is the oxidation time and n is the time exponent. Kinetic data for the alloys can be seen in **Table 46.**1. The TaTiCr alloy showed one distinct near-cubic regime of kinetics for the duration of the test. Both Ta_4Ti_3Cr and Ta_2TiCr primarily display singular near-linear regimes of; however, the kinetics of Ta_2TiCr deviate from linearity and become slower as it approaches complete oxidation (after ~12 hours). Ta_4TiCr_3 has a different behavior compared to all other alloys, starting with a parabolic regime up to 9 hours, which then transitions into a near-linear regime from 9-16 hours, followed by a final linear regime until the end of the test (24 hours).

Table 46.1: Oxidation kinetic data for the four alloys

Alloy	Mass gain after 24 hrs (mg/cm^2)	k (mg/cm^2-h^n)	n	Segment
TaTiCr	7.2	3.58	0.23	0-24 hrs
Ta_4Ti_3Cr	124.1	7.88	0.85	0-24 hrs
Ta_2TiCr	160.9	12.06	1.03	0-24 hrs
Ta_4TiCr_3	71.5	3.55	0.51	0-10 hrs
		0.84	1.17	10-22 hrs
		0.01	3.19	22-24 hrs

46.3.2 Post-oxidation Microstructure

The post-oxidation specimens were analyzed using BSE imaging, XRD, and EDS to investigate oxide morphologies, oxide products, and microstructural changes after oxidation to correlate microstructure and composition to oxidation performance. As shown by the cross-sectional view in **Figure 46.3a**, the TaTiCr alloy formed a multi-layered, outer oxide scale that was adherent and showed no visible spallation after 24 hours of oxidation. The outer scale thickness was 30µm. Below this outer layer, a pronounced internal reacted zone (IRZ) was observed (**Fig. 46.3b**). This layer was approximately 170µm thick and consisted of a BCC matrix with Laves particles with the addition of a dark, lenticular phase that formed between the two phases. The center (**Fig. 46.3c**) of the specimen remained BCC + Laves, with no evidence of oxides forming or oxygen diffusion. However, the Laves particles in the sample core became more globular after the high temperature exposure.

The Ta_4Ti_3Cr alloy cross section (**Fig. 46.3d**) shows that the alloy formed a thick porous oxide scale, measuring 1.29mm. Near the oxide-metal interface (**Fig. 46.3e**), dark, needle-like precipitates grew during the oxidation tests, with a very fine morphology within the grains and a much coarser morphology along grain boundaries. These dark grain boundary precipitates continue into the center of the specimen (**Fig. 46.3f**), suggesting the entire internal area had reacted to some extent.

The Ta_2TiCr alloy formed a thick, porous scale that showed significant separation from the metal-oxide interface (**Fig. 46.3g**) after 13 hours. This outer oxide scale was roughly 1.15mm thick. The IRZ (**Fig. 46.3h**) was approximately 150µm thick and was similar to the starting microstructure, with the addition of a dark precipitate phase that formed along primary and secondary Laves phase boundaries, as well as fine, acicular precipitates that grew in the BCC matrix. The unreacted center of the specimen (**Fig. 46.3i**) remained BCC + Laves, with some coalescence and growth of the primary Laves and dissolution of secondary Laves, due to the high temperature exposure.

The cross-section of the Ta_4TiCr_3 alloy shows that the alloy formed a thick, porous scale, similar to Ta_2TiCr, that lost adhesion with the metal-oxide interface (**Fig. 46.3j**) after 24 hours. The scale was 600µm thick on average. The IRZ (**Fig. 46.3k**) was approximately 100µm thick and had similar features as Ta_2TiCr, with dark precipitate phases that formed along primary and secondary Laves phase boundaries. Dark, globular precipitates were also seen in the matrix. The unreacted center (**Fig. 46.3l**) of the specimen remained BCC+Laves, with an increased phase fraction of secondary Laves precipitates after oxidation (0.055 to 0.078).

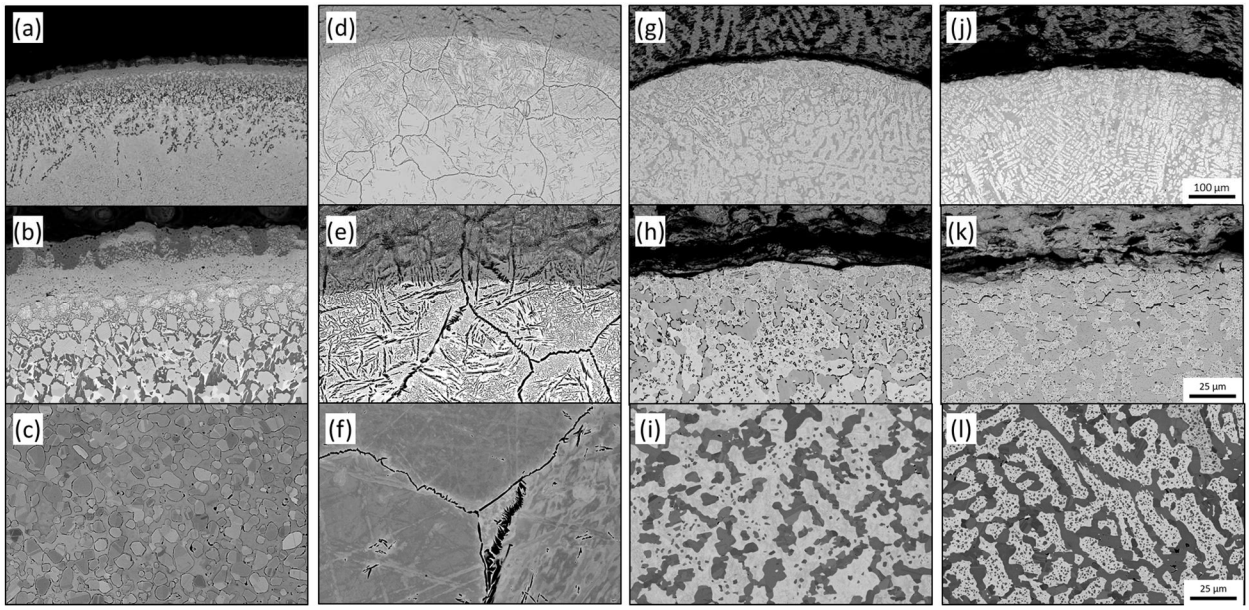

Figure 46.3: Backscatter SEM images of the microstructure of the four alloys after oxidation tests: (a,b,c) TaTiCr, (d,e,f) Ta_4Ti_3Cr, (g,h,i) Ta_2TiCr, and (j,k,l) Ta_4TiCr_3. Scale bars are consistent across each horizontal row

46.3.3 Oxide Products and Morphologies

XRD spectra captured from the oxide scale powder of the four alloys after 24 hours is shown in **Figure 46.4**. Several mixed "rutile" (P42/mnm, SG 136) complex oxide structures were seen in all alloys: $(Cr,Ta,Ti)_2O_4$ was observed in all four alloys (**Fig. 46.4a-d**); $TaTiO_4$ was seen in TaTiCr, Ta_4Ti_3Cr, and Ta_2TiCr (**Fig. 46.4a-c**); TiO_2 was seen in TaTiCr and $Ta4Ti_3Cr$ (**Fig. 46.4a-b**); $CrTaO_4$ was observed in Ta_2TiCr and Ta_4TiCr_3 (**Fig. 46.4c-d**); and $CrTiO_4$ was seen in TaTiCr only (**Fig. 46.4a**). Similar mixed structures have been seen in the CrNbTi and CrNbTaTi system by Butler, et al. [46.8] and were reported to be caused by competitive oxide formation driven from the high concentration of alloying additions. This ultimately leads to shared occupancy within the rutile cation sublattice. Additionally, peaks associated with Cr_2O_3 (R-3c, SG 167) were seen in TaTiCr and Ta_4TiCr_3 (**Fig. 46.4a, 46.4d**); Ta_2O_5 (I/4mmm, SG 139) was observed in all but TaTiCr (**Fig. 46.4b-d**); and Ta_4Ti_3Cr showed peaks coinciding with Ta_2TiO_7 (I 12/m 1, SG 12).

EDS maps of the alloy cross sections show the various oxide products and unique oxide morphologies seen in each alloy. The external oxide scale (**Fig. 46.5a**) in TaTiCr consisted of an outer Ti-rich layer (**Fig. 46.5a, marker 1**), an intermediate Cr-rich layer (**Fig. 46.5a, 2**), and an inner layer consisting primarily of Ta (**Fig. 46.5b**) and Ti (**Fig. 46.5c**), with a Cr composition gradient initiating from the intermediate layer (**Fig. 9d**). Regions 1 and 2 exhibited chemistries consistent with TiO_2 and Cr_2O_3, respectively (**Table 46.2**). The innermost oxide layer exhibited multiple chemistries cascading from the Cr_2O_3 layer: $CrTiO_4$ (**Fig. 46.5a, 3**), $(Cr,Ta,Ti)_2O_4$ (**Fig. 46.5a, 4**), and $TaTiO_4$ (**Fig. 46.5a, 5, and Table 46.2**). At the metal-oxide interface, Ta-rich particles with chemistry similar to Ta_2O_5 (**Fig. 46.5a, 6**) can be found which appear to be prior-Laves particles that have reacted after rejecting all Cr and Ti to the oxide scale. In the IRZ, the lenticular phase is Ti- and N-rich with a chemistry similar to TiN (**Fig. 46.5a,7**). The Cr-rich particles are unreacted Laves (**Fig.46.5a, 8**) and the BCC matrix (**Fig. 46.5a, 9**) was Ta-rich due to Ti rejection from the matrix to form TiN. This is consistent with the higher Ti concentration in the prior BCC phase compared to Laves, Table 46.2. A Ti-rich phase with chemistry consistent with the HCP (α) phase is present near the internal oxidation front of the IRZ (**Fig. 46.5a, 10**). The majority of O-enrichment remained in the oxide scale, with some O-enrichment seen in the IRZ (**Fig 46.5e**), most notably segregated to Laves particles. N-enrichment was exclusively seen in the Ti-rich regions in the IRZ (**Fig. 46.5f**).

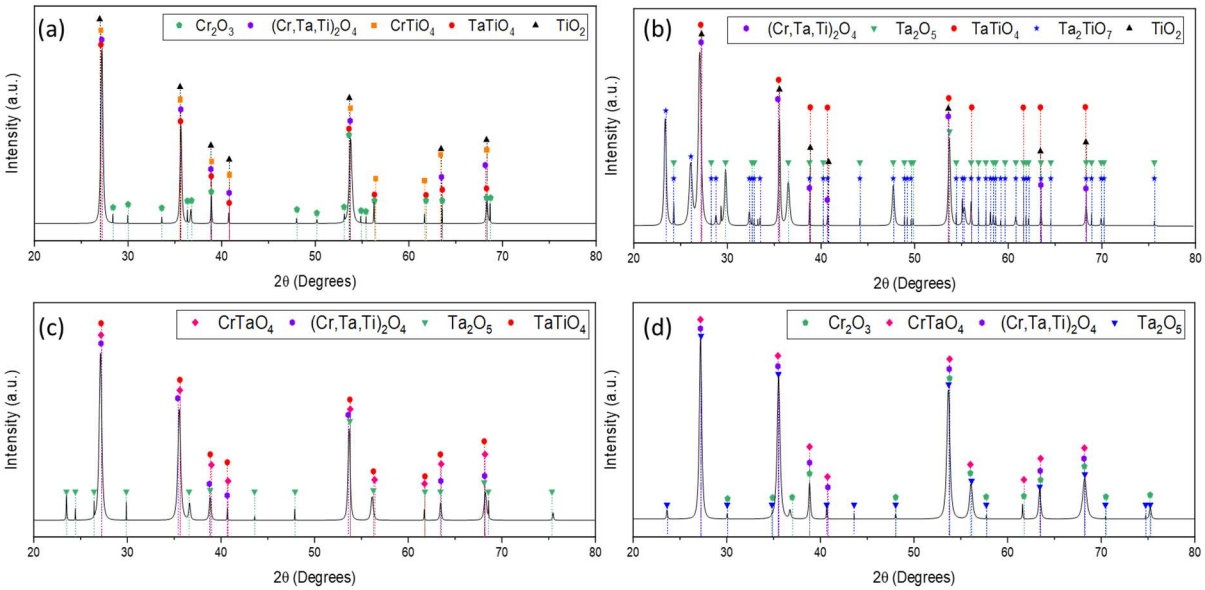

Figure 46.4: XRD spectra captured from the (a) TaTiCr, (b) Ta_4Ti_3Cr, (c) Ta_2TiCr, and (d) Ta_4TiCr_3 alloys after oxidation at 1200 °C for 24 hrs.

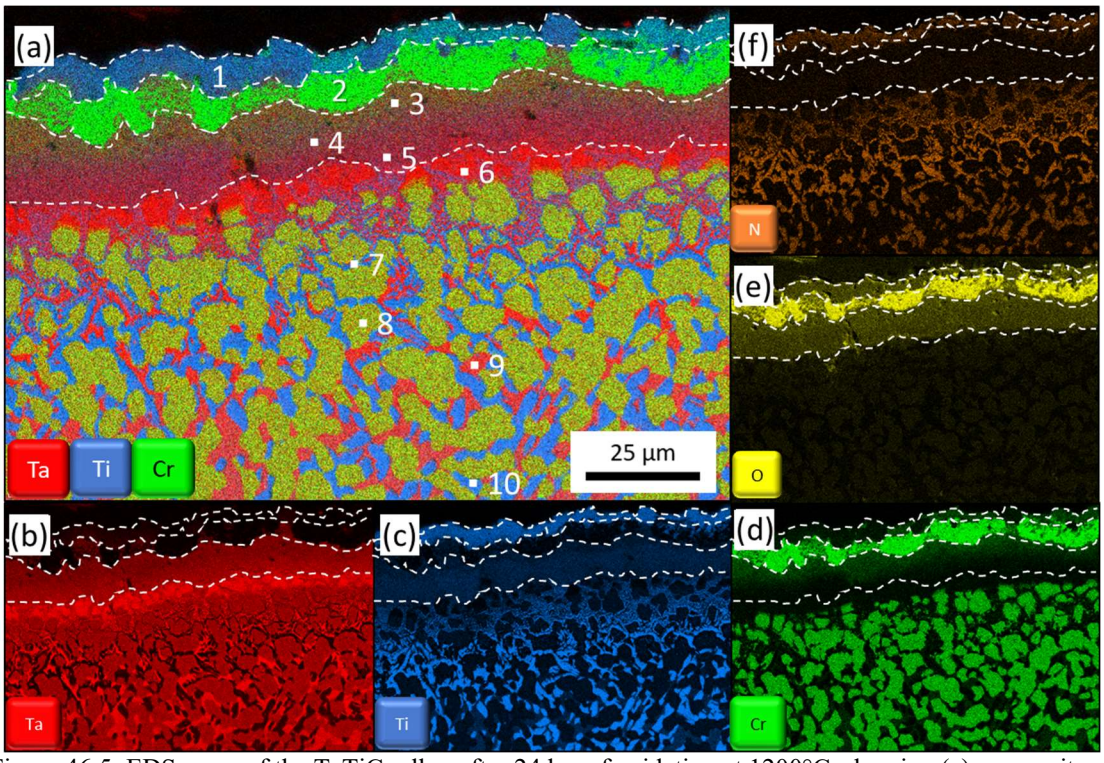

Figure 46.5: EDS maps of the TaTiCr alloy after 24 hrs of oxidation at 1200°C, showing (a) composite map of the alloying elements, (b) Ta, (c) Ti, (d) Cr, (e) O, (f) N content in the alloy.

Table 46.2 Observed phases in the TaTiCr alloy after oxidation at 1200°C for 24 hrs.

Region	Marker (Fig. 46.5)	Phase
External Oxides	**1**	TiO_2
	2	Cr_2O_3
	3	$CrTiO_4$
	4	$(Cr,Ta,Ti)_2O_4$
	5	$TaTiO_4$
IRZ	**6**	Ta_2O_5
	7	Laves
	8	BCC
	9	TiN
	10	HCP

The outer oxide scale of the Ta_4Ti_3Cr alloy (**Fig. 46.6a**) consisted of a repeating structure whose morphology transitions to resemble that of the post-oxidation microstructure near the metal-oxide interface. The bulk of the oxide consists of three distinct oxide structures. Region 1 in the scale has chemistry consistent with Ta_2TiO_7 (**Fig. 46.6a, Table 46.3**), the Ta-rich "pockets" in region 2 were measured to be Ta_2O_5 (**Fig. 46.6a, Table 46.3**), and the repeating structure in region 3 was measured as $(Cr,Ta,Ti)_2O_4$ (**Fig. 46.6a, Table 46.3**). The repeating morphology is suggestive of local solute depletion phenomena, causing multiple recursive oxidation reactions to occur and repeat as specific constituents are selectively oxidized. Near the oxide-IRZ interface, the scale is primarily Ta-rich (**Fig. 46.6b**), with Ti-rich (**Fig. 46.6c**) bands streaking out from the dark precipitates in the metal substrate. Small, discontinuous Cr-rich (**Fig. 46.6d**) regions are dispersed throughout the scale. EDS measurements on region 4 revealed that the Ti-rich region chemistry isTiO_2, confirming the XRD observations. There is a distinct region of O-enrichment (**Fig. 46.6e**) in the oxide scale directly below the N-rich layer (**Fig. 46.6f**), where dark precipitates reside both within the grains and along the grain boundaries. Region 5 was measured to be TiN. The dark precipitates **(Fig. 46.6b, 7**) are Ti-rich and are likely oxygen-stabilized HCP. These precipitates are morphologically similar to α-Ti precipitate structures present in many β-Ti alloys, including Ti-5Al-5Mo-5V-3Cr (Ti-5553). Small Laves precipitates were seen along the grain boundary HCP, seen in region 8 (**Fig. 46.6b, Table 46.3**). Below this, the BCC matrix remained Ta-rich; however, the Ti content was depleted in comparison to the pre-test composition.

Figure 46.7 shows a composite EDS map of the Ta_2TiCr oxide scale after a 13-hour oxidation test. The external oxide scale consisted of a periodic layered structure of similar morphology to Ta_4Ti_3Cr. The repeating structure shown by region 1 was measured to be $(Cr,Ta,Ti)_2O_4$, with Ta_2O_5 pockets (**Fig. 46.7a, 2**) surrounded by regions of $TaTiO_4$ (**Fig. 46.7a, 3, and Table 46.4**). Near the oxide-IRZ interface (**Fig. 46.7b**), the scale was mostly Ta-rich (**Fig. 46.7c**), with layers of Ti enrichment (**Fig. 46.7d**) and Cr enrichment (**Fig. 46.7e**). Unlike the previous alloys, oxygen remained almost exclusively in the external scale and there was very little retained in the metal substrate (**Fig. 46.7f**). At the metal-oxide interface there is a slightly N-rich region with small, Ti-rich particles dispersed throughout (**Fig. 46.7g**), EDS confirmed the chemistry to be TiN (**Fig. 46.7b, 4**). **Figure 46.7b, markers 5 and 6** are Laves and BCC, respectively. Deeper into the IRZ, small Ti-rich precipitates were in the matrix. These particles have chemistry consistent with HCP Ti (**Fig. 46.7b, 7, and Table 46.4**). Below the N-rich region, a Ti-depleted zone can be seen (**Fig. 46.7d**).

The surface of the oxide scale of the Ta_4TiCr_3 alloy (**Fig. 46.8a**) appeared to have consisted of a layered structure, with a Cr_2O_3 outer layer (**Fig. 46.8a, 1**), $CrTaO_4$ middle layer (**Fig. 46.8a, 2**) and large, Ta_2O_5 structures (**Fig. 46.8a, 3**) atop a layer of $(Cr,Ta,Ti)_2O_4$ (**Fig. 46.8a, 4**). This section was separated from the bulk oxide (**Fig. 46.8b**), likely due to the rumpling effects and oxide growth. The bulk oxide scale again consisted of a periodic layered structure **(Fig. 46.8b**) that had similar chemistries to the surface in vastly different morphologies. The majority of the scale consisted of $CrTaO_4$ (**Fig. 46.8b, 2**), with Ta_2O_5 pockets (**Fig. 46.8b, 3**) surrounded by small areas of $(Cr,Ta,Ti)_2O_4$ (**Fig. 46.8b, 4**). Thin bands of Cr_2O_3 were seen (**Fig. 46.8b, 1**), indicating the periodicity of the scale. Near the

surface, the scale was mostly Ta-rich (**Fig. 46.8c, 46.8d**), with layers of Cr-enrichment (**Fig. 46.8f**). The discontinuous Cr-rich regions had a chemistry consistent with Cr_2O_3, followed by Ta_2O_5 (**Table 46.5**). The fine, dark globular precipitates in the matrix are likely HCP. The Ti-rich dark precipitates surrounding the Laves particles are TiO_2 (**Fig. 46.8c, 5**), differing from the other alloys**. Fig. 46.8c, regions 6 and 7** were measured to be BCC and Laves, respectively (**Table 46.5**). Similar to Ta_2TiCr, there was minimal oxygen (**Fig. 46.8g**) retention in the metal, and very small dispersions of nitrogen (**Fig. 46.8h)** near the metal-oxide interface.

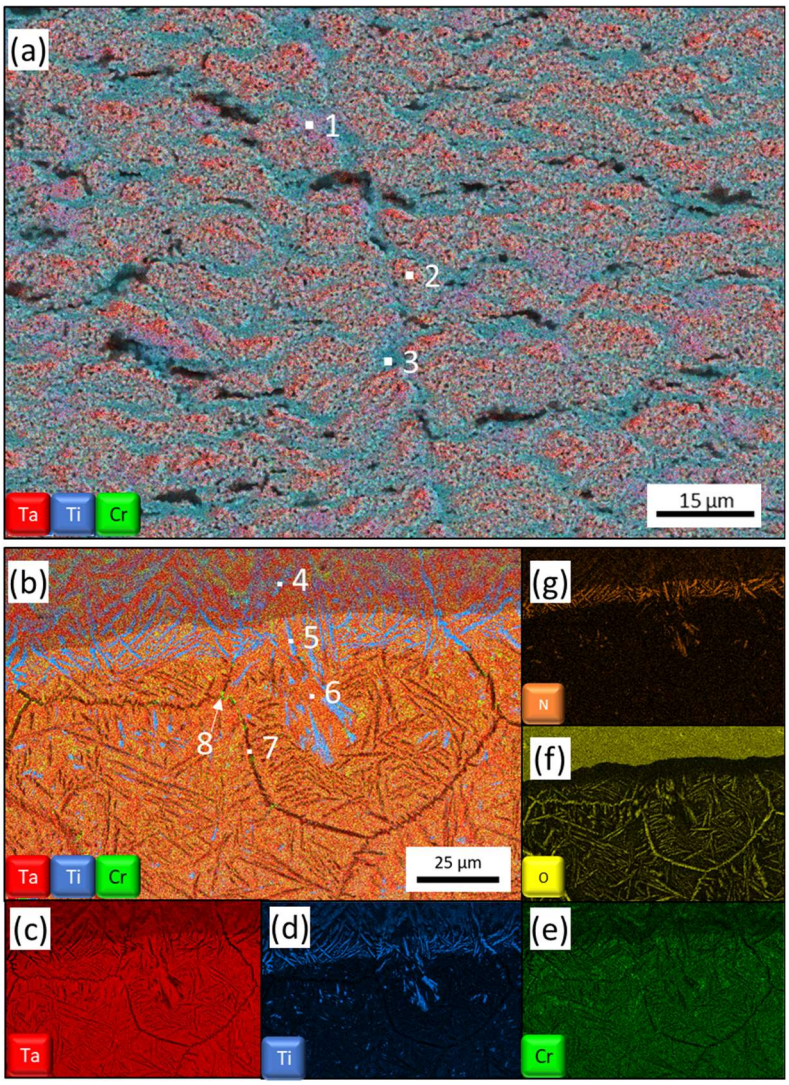

Figure 46.6: EDS maps of the Ta_4Ti_3Cr alloy after 24 hrs of oxidation at 1200°C, showing a composite map of the (a) oxide scale, (b) IRZ, (c) Ta, (d) Ti, (e) Cr, (f) O, (g) N content in the alloy.

Table 46.3: EDS measurements for the observed phases in the Ta_4Ti_3Cr alloy after oxidation at 1200 °C for 24 hrs.

Region	Marker	Phase	Cr	Ta	Ti	O	N
External Oxides	1	Ta_2TiO_7	0.1	18.7	10.9	69.6	
	2	Ta_2O_5	1.1	23.4	4.5	70.5	-
	3	$(Cr,Ta,Ti)_2O_4$	7.9	6.5	18.7	66.9	
	4	TiO_2	3.3	6.3	23.2	67.2	
IRZ	5	TiN	2.5	3.5	41.4	-	52.6
	6	BCC	8.6	62.9	20.5	8.0	-
	7	HCP	2.0	3.9	67.8	23.4	3.0
	8	Laves	53.0	35.5	11.5	-	-

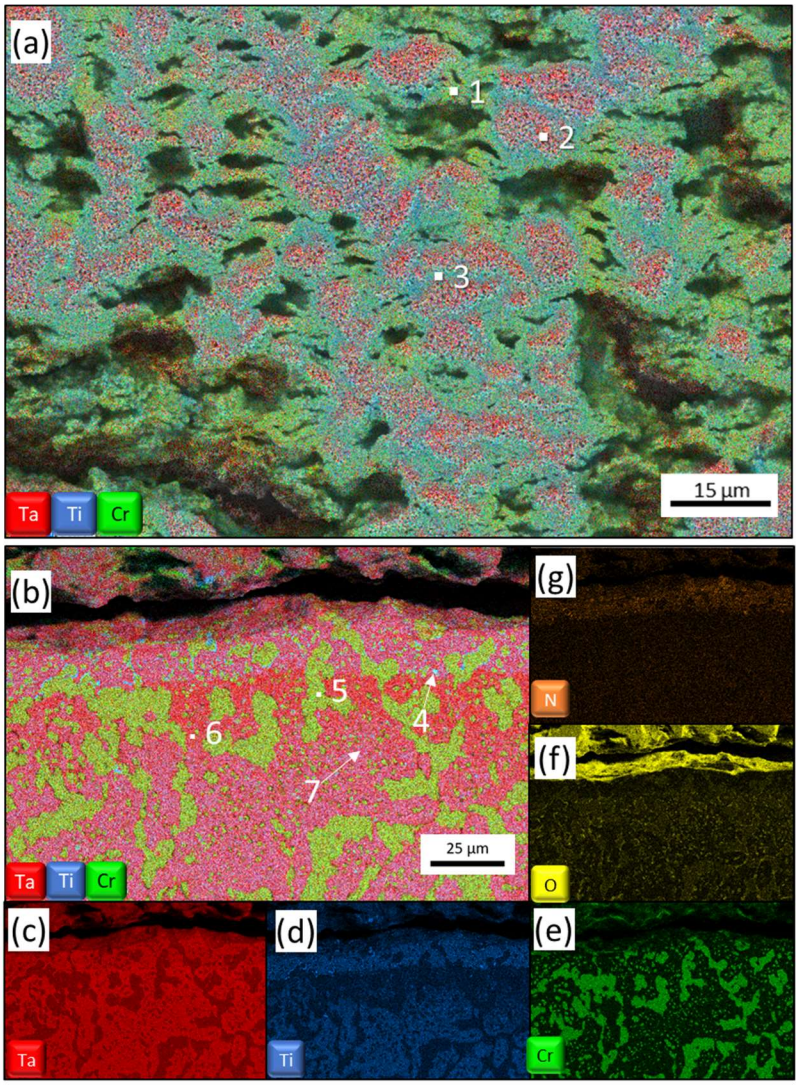

Figure 46.7: EDS maps of the Ta_2TiCr alloy after 13 hrs of oxidation at 1200°C, showing a composite map of the (a) oxide scale, (b) IRZ, (c) Ta, (d) Ti, (e) Cr, (f) O, (g) N content in the alloy.

Table 46.4: EDS measurements for the observed phases in the Ta_2TiCr alloy after oxidation at 1200 °C for 24 hrs.

Region	Marker	Phase	Cr	Ta	Ti	O	N
External Oxides	**1**	$(Cr,Ta,Ti)_2O_4$	9.2	9.8	11.4	69.6	-
	2	Ta_2O_5	0.6	23.7	0.5	75.3	-
	3	$TaTiO_4$	5.5	11.3	15.5	67.6	-
IRZ	**4**	Laves	53.0	29.4	17.6	-	-
	5	TiN	2.1	10.9	53.6	4.4	29.0
	6	BCC	9.7	62.5	22.4	5.3	-
	7	HCP	2.0	8.2	70.6	19.2	-

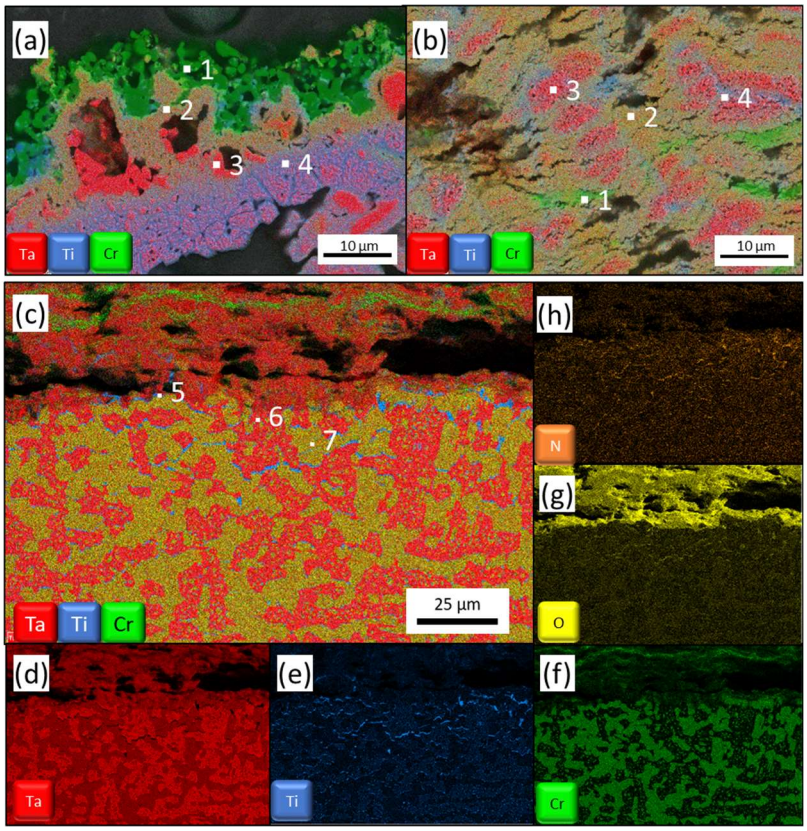

Figure 46.7: EDS maps of the Ta_4TiCr_3 alloy after 24 hrs of oxidation at 1200°C, showing a composite map of the (a) surface oxide scale, (b) bulk oxide scale, (c) IRZ, (d) Ta, (e) Ti, (f) Cr, (g) O, (h) N content in the alloy.

Table 46.5: EDS measurements for the observed phases in the Ta_4TiCr_3 alloy after oxidation at 1200 °C for 24 hrs.

Region	Marker	Phase	Cr	Ta	Ti	O	N
External Oxides	1	Cr_2O_3	38.1	0.3	1.3	60.3	-
	2	$CrTaO_4$	14.9	15.3	3.2	66.7	-
	3	Ta_2O_5	0.4	28.3	-	71.3	-
	4	$(Cr,Ta,Ti)_2O_4$	10.2	13.0	9.6	67.1	-
IRZ	5	TiO_2	5.3	7.7	45.7	41.3	-
	6	BCC	5.1	64.6	10.6	-	19.7
	7	Laves	62.9	34.8	2.3	-	-

46.4 Plans for Next Reporting Period

Next, reporting period, the following items are planned to be underway or completed:

- Compression tests to assess mechanical behavior of the four alloys.
- Use AM (LENS) to print Ta-lean and/or Ti-rich compositions to investigate additive manufacturing processing effects on microstructure, as well as oxidation performance on compositionally graded alloys.
- Investigate the effect of Laser Shock Peening (LSP) on surface microstructure and oxidation performance and its effects for surface recrystallization.

46.5 References

[46.1] D.B. Miracle, O.N. Senkov (2017). A critical review of high entropy alloys and related concepts. Acta Materialia. Volume 175.

[46.2] O.N. Senkov, et al. (2019). High Temperature Strength of Refractory Complex Concentrated Alloys. Acta Materialia. Volume 175.

[46.3] D.B. Miracle, O.N. Senkv (2019). Refractory Complex Concentrated Alloys (RCCAs). ARPA-E Workshop, Air Force Research Laboratory

[46.4] T.M. Butler, et al. (2017). High temperature oxidation behaviors of equimolar NbTiZrV and NbTiZrCr refractory complex concentrated alloys (RCCAs). Journal of Alloys and Compounds.

[46.5] O.N. Senkov, D.B. Miracle, K.J. Kaput et al. (2018). Development and exploration of refractory high entropy alloys—A review. Journal of Materials Research 33, 3092–3128.

[46.6] S. Gorsse, M.H. Nguyen, O.N. Senkov D.B. Miracle, (2018). Database on the mechanical properties of high entropy alloys and complex concentrated alloys. Data in Brief. Volume 21.

[46.7] B. Martin, Development of a Novel, Bicombinatorial Approach to Alloy Development, and Application to Rapid Screening of Creep Resistant Titanium Alloys, (2017). Graduate Theses and Disstertaions. Iowa State University.

[46.8] T.M. Butler, et al. (2021). Oxidation behaviors of CrNb, CrNbTi, and CrNbTaTi concentrated refractory alloys. Intermetallics. Volume 140.